

1 Multiplexed imaging of human tuberculosis granulomas uncovers 2 immunoregulatory features conserved across tissue and blood

3
4 Erin F. McCaffrey¹, Michele Donato^{2,3}, Leeat Keren¹, Zhenghao Chen⁴, Megan
5 Fitzpatrick⁵, Vladimir Jovic⁴, Alea Delmastro¹, Noah F. Greenwald¹, Alex Baranski¹,
6 William Graf⁶, Marc Bosse¹, Pratista K. Ramdial^{7,8}, Erna Forgo¹, David Van Valen⁶, Matt
7 van de Rijn¹, Sean C. Bendall¹, Niaz Banaei^{1,9}, Adrie J.C. Steyn^{6,10}, Purvesh Khatri^{2,3}, &
8 Michael Angelo¹

9
10 ¹Stanford University Department of Pathology; ²Stanford Center for Biomedical
11 Informatics Research; ³Stanford Institute for Immunity, Transplantation and Infection;
12 ⁴Calico Life Sciences LLC; ⁵University of Wisconsin, Department of Pathology; ⁶Division
13 of Biology and Bioengineering, California Institute of Technology; ⁷African Health
14 Research Institute; ⁸University of KwaZulu-Natal, Inkosi Albert Luthuli Central Hospital
15 ⁹Stanford University Department of Medicine-Infectious Diseases; ¹⁰Department of
16 Microbiology, University of Alabama at Birmingham

17
18

19 **Abstract**

20 Tuberculosis (TB) is an infectious disease caused by *Mycobacterium tuberculosis*
21 that is distinctly characterized by granuloma formation within infected tissues.
22 Granulomas are dynamic and organized immune cell aggregates that limit dissemination,
23 but can also hinder bacterial clearance. Consequently, outcome in TB is influenced by
24 how granuloma structure and composition shift the balance between these two functions.
25 To date, our understanding of what factors drive granuloma function in humans is limited.
26 With this in mind, we used Multiplexed Ion Beam Imaging by Time-of-Flight (MIBI-TOF)
27 to profile 37 proteins in tissues from thirteen patients with active TB disease from the U.S.
28 and South Africa. With this dataset, we constructed a comprehensive tissue atlas where
29 the lineage, functional state, and spatial distribution of 19 unique cell subsets were
30 mapped onto eight phenotypically-distinct granuloma microenvironments. This work
31 revealed an immunosuppressed microenvironment specific to TB granulomas with
32 spatially coordinated co-expression of IDO1 and PD-L1 by myeloid cells and proliferating
33 regulatory T cells. Interestingly, this microenvironment lacked markers consistent with T-
34 cell activation, supporting a myeloid-mediated mechanism of immune suppression. We
35 observed similar trends in gene expression of immunoregulatory proteins in a
36 confirmatory transcriptomic analysis of peripheral blood collected from over 1500

37 individuals with latent or active TB infection and healthy controls across 29 cohorts
38 spanning 14 countries. Notably, PD-L1 gene expression was found to correlate with TB
39 progression and treatment response, supporting its potential use as a blood-based
40 biomarker. Taken together, this study serves as a framework for leveraging independent
41 cohorts and complementary methodologies to understand how local and systemic
42 immune responses are linked in human health and disease.

43

44 **Introduction**

45 *Mycobacterium tuberculosis* (*Mtb*) is the leading cause of mortality from infectious
46 disease in the world, accounting for nearly 1.5 million deaths each year¹. Relative to other
47 communicable diseases, the reduction in the incidence of TB infection over the last 20
48 years has been modest. This is largely due to the lack of a highly efficacious vaccine,
49 lengthy and toxic antimicrobial regimens, and emergence of multidrug resistance. Along
50 these lines, previous efforts to develop new host-directed therapies have been hindered
51 by an incomplete understanding of how TB interacts with the human immune system
52 during infection.

53 Infection is initiated when bacteria are engulfed by alveolar macrophages or other
54 resident phagocytes after being inhaled into the lungs^{2,3}. This triggers an immune
55 response that ultimately converges on formation of a granuloma, a dynamic and spatially-
56 organized tissue structure comprised of macrophages, granulocytes, lymphocytes, and
57 fibroblasts. A prototypical non-necrotic granuloma consists of a myeloid-predominant
58 central core region that is enriched with infected macrophages and encircled by
59 lymphocytes. From the perspective of facilitating an effective host response, granulomas
60 play seemingly contradictory roles. On the one hand, consolidation of infected cells within
61 the myeloid core limits dissemination by partitioning them away from uninvolved lung
62 parenchyma. On the other, tolerogenic pathways that are upregulated within this region
63 limit bacterial clearance⁴⁻⁶.

64 Depending on the histological subtype and bacterial burden, granuloma
65 composition can be highly variable⁷. This variability can manifest within a single individual,
66 where infection can result in formation of multiple granulomas with distinct histologic and

67 immunological features that each progress independently of one another over time⁸.
68 Controlled infections in non-human primates (NHP) have revealed that a single individual
69 can possess well over ten granulomas and that the inflammatory profile, size, and
70 bacterial ecology of these lesions can vary dramatically^{9–11}. Thus, the trajectory of each
71 granuloma can vary across a spectrum between complete bacterial clearance to
72 uncontrolled dissemination. This discordance suggests that local host-bacterial dynamics
73 within the tissue microenvironment play a central role in determining granuloma fate.
74 Along these lines, a growing number of studies suggest that granuloma structure and
75 immune cell function are interconnected^{12,13}. For example, previous work has suggested
76 that impaired adaptive immunity might be the consequence of T cells being largely
77 excluded from the myeloid-dominated central core region where infected macrophages
78 tend to localize^{14,15}.

79 Taken together, these findings suggest that TB disease progression is heavily
80 impacted by focal, spatially-encoded regulatory mechanisms within the granuloma
81 microenvironment. Consequently, understanding how these mechanisms promote
82 bacterial clearance or persistence is critical for designing effective therapies that promote
83 long term immunity. With this in mind, we used Multiplexed Ion Beam Imaging by Time-
84 of-Flight (MIBI-TOF) to simultaneously image 37 proteins at subcellular resolution in solid
85 tissue from individuals with active TB infection¹⁶. We compared granuloma composition
86 with respect to 19 unique cell subsets to delineate different subtypes of granulomas that
87 were enriched for classical monocytes, myeloid-derived suppressor cell-like (MDSC)
88 macrophages, or tertiary lymphoid structures (TLS). We then utilized an adaptation of
89 Latent Dirichlet Allocation (spatial-LDA) to identify spatially-coordinated immune
90 responses within eight recurrent cellular microenvironments. These analyses revealed a
91 microenvironment characterized by expression of regulatory proteins, IDO1 and PD-L1,
92 and proliferative regulatory T cells. Paradoxically, these cells were not accompanied by
93 significant numbers of PD-1⁺ lymphocytes or any other evidence suggesting T cell
94 exhaustion.

95 To determine if these features were associated with drug treatment or severity of
96 infection, we leveraged publicly available gene expression data of peripheral blood from

97 patients with TB. In line with the granuloma imaging data, we found increased expression
98 of *IDO1* and *CD274* (PD-L1) and diminished expression of *PDCD1* (PD-1) and *LAG3* in
99 individuals with active TB. Moreover, *CD274* (PD-L1) gene expression was found to
100 associate with progression from latent to active disease and with therapeutic response,
101 suggesting it could be used as a novel prognostic biomarker. Taken together, this work
102 provides compelling evidence for a myeloid-mediated mechanism of immune suppression
103 driven locally within the granuloma that promotes bacterial persistence and subverts T-
104 cell activation.

105

106 **Results**

107 [Multiplexed imaging of human tuberculosis granulomas reveals structured immune cell](#) 108 [composition](#)

109 To assess granuloma composition and architecture in TB, we curated a cohort of
110 actively infected human tissues. Archival formalin-fixed paraffin-embedded (FFPE)
111 specimens from patients treated in the United States or South Africa were procured from
112 Stanford Health Care or University of KwaZulu-Natal, Inkosi Albert Luthuli Central
113 Hospital, respectively (Extended Data Table 1). The South African samples were
114 pulmonary tissues from patients that underwent therapeutic resection for advanced TB (n
115 = 6). While TB disease typically manifests in the lung, infection can disseminate to extra-
116 pulmonary sites as well^{17,18}. To characterize TB infection at an earlier stage and assess
117 how granuloma composition varies with infection site, samples from US patients
118 consisted of diagnostic biopsies from lung (n = 2), pleural cavity (n = 3), lymph node (n =
119 1), and endometrium (n = 1) (Fig. 1a).

120 Tissue sections for each specimen were reviewed by an anatomic pathologist and
121 screened to include the presence of solid, non-necrotic granulomas or active
122 granulomatous inflammation, while excluding excessively necrotic or fibrotic regions
123 (Extended Data Fig. 1a). MIBI-TOF was subsequently used to image two 500 μm^2 fields
124 of view (FOVs) per tissue stained with a 37-plex panel of metal-labeled antibodies (Fig.
125 1b, Extended Data Fig. 1b-c, Extended Data Table 2)¹⁶. The antibody panel included
126 markers to comprehensively phenotype most major immune and non-immune cell

127 lineages, including lymphocytes, macrophages, granulocytes, stroma, and epithelium.
128 The panel also included antibodies for 12 functional markers with an emphasis on those
129 with well-documented immunoregulatory pathways, including PD-1, Lag3, PD-L1, and
130 IDO1.

131 To extract single cell phenotypes, multiplexed imaging data were processed with
132 a low-level pipeline prior to single-cell segmentation (Fig. 1a, Extended Data Fig. 1d)^{19–}
133 ²¹. Each FOV contained an average of ~1400 single cells (sd = 312) (Extended Data Fig.
134 2d). Hierarchical application of the FlowSOM algorithm (Extended Data Fig. 2a, b) was
135 employed to phenotype 19 unique cell subsets (Fig. 1c)²² using cell area normalized
136 values of protein expression for each segmented cell event. For each image, FlowSOM
137 clusters and segmentation masks were combined to generate cell phenotype maps
138 (CPM) where each cell is labeled by its phenotype (Fig. 1d, Extended Data Fig. 2c).

139 Consistent with previous work, granuloma composition was predominated in most
140 lesions by T cells and myeloid cells, (average myeloid: lymphoid ratio = 1.4, sd = 1.0)²³.
141 Myelomonocytic cells were comprised of multiple subsets of macrophages, dendritic cells,
142 and monocytes that were each distinguished by varying degrees of co-expression of
143 CD11c, CD11b, CD209, CD68, CD14, CD16, and CD206 (Fig. 1e). Granulocytes were
144 comprised largely of neutrophils (mean = 1.2%, sd = 1.7) and mast cells ($0.6\% \pm 0.8$)^{24–}
145 ²⁶. We also identified $\gamma\delta$ T cells ($0.1\% \pm 0.22$), CD209⁺ dendritic cells ($0.2\% \pm 0.5$), and
146 regulatory T cells ($0.4\% \pm 0.6$), highlighting the capability of our approach to enumerate
147 low abundance immune cell populations that have been suggested to play a key role in
148 granuloma pathology. In line with reports of increased vascularization in active disease,
149 non-immune cells were predominated by endothelial cells ($5.7\% \pm 3.1$) while fibroblasts
150 ($3.3\% \pm 5.1$) and epithelial cells ($2.7\% \pm 4.0$) varied significantly between lesions
151 (Extended Data Fig. 2e, f)^{27,28}. Altogether, we assigned 94% (n = 33,194 single cells) of
152 cells to 19 subsets that in aggregate ranged in frequency from 0.1-15% across our
153 dataset.

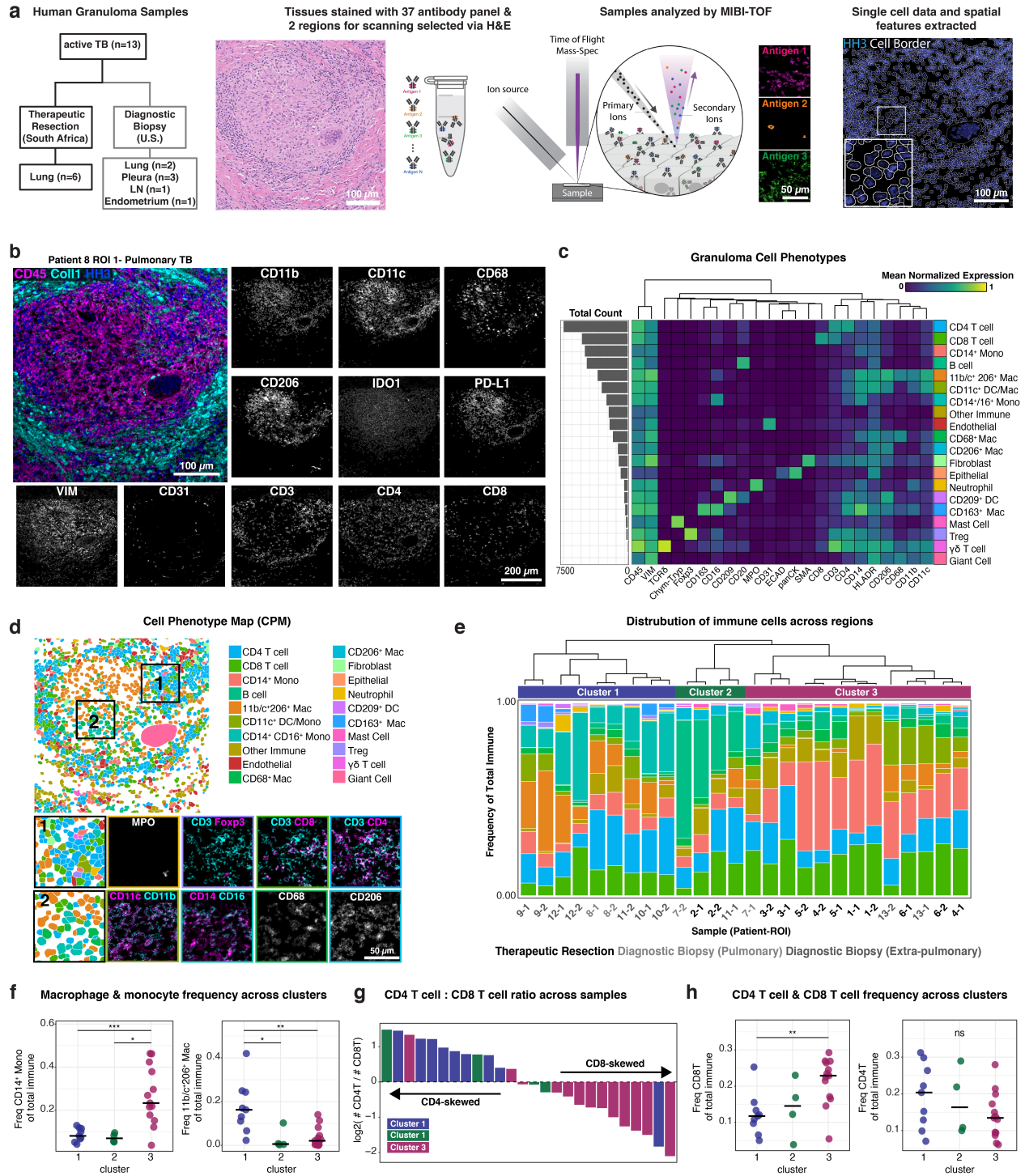


Figure 1. Multiplexed imaging of human tuberculosis granulomas reveals structured immune cell composition. (a) Conceptual overview of MIBI-TOF analysis of human TB granulomas. (b) Representative images from a pulmonary TB section. (c) Cell lineage assignments based on normalized expression of lineage markers (heatmap columns). Rows are ordered by absolute abundance shown on the bar plot (left), while columns are hierarchically clustered (Euclidean distance, average linkage). (d) Cell identity overlaid onto the segmentation mask for a representative pulmonary TB section (left). Two insets (bottom) are shown. (e) The relative abundance of immune cell types across all TB FOVs with

cell types ordered by decreasing median abundance and bars ordered by the hierarchical relationship of pairwise Pearson correlation coefficients (distance = 1 – correlation, complete linkage). Consensus clusters are annotated above bar plot (cluster 1 = blue, cluster 2 = green, cluster 3 = purple). **(f)** Frequency of CD14⁺ monocytes and 11b/c⁺ 206⁺ macrophages of total immune cells colored by cluster. Line represents the median. **(g)** The CD4 T: CD8 T cell ratio represented as a log₂ fold-change for each TB FOV (top) colored by cluster. **(h)** Frequency of CD4⁺ and CD8⁺ T cells of total immune cells colored by cluster. Line represents the median. All p-values determined with a Wilcoxon Rank Sum Test where: ns p > 0.05, * p < 0.05, ** p < 0.01, *** p < 0.001.

154

155 To assess whether granulomas can be grouped into subtypes based exclusively
156 on immune cell subset frequencies, we clustered FOVs using Pearson correlation based
157 on their immune cell proportions (Extended Data Fig. 2g). We found that using three
158 clusters explained 72% of the variance in our dataset (Fig. 1e, Extended Data Fig. 2h).
159 Cluster 1 (Fig. 1e, f) was characterized by CD11c⁺ CD11b⁺ macrophages, intermediate
160 monocytes, and occasional CD163⁺ macrophages. Chi-square analysis of cell type co-
161 occurrence showed significant associations of CD163⁺ macrophages with intermediate
162 monocytes (adj. p = 0.0090), regulatory T cells (Tregs) (adj. p = 0.003), and fibroblasts
163 (adj. p = 0.02), suggesting coordinated cellular presence in this cluster (Extended Data
164 Fig. 2i). Cluster 2 was enriched for B cells (Fig. 1e). Lastly, a subset of granulomas
165 (cluster 3) was enriched for classical monocytes (Fig. 1e, f) and higher numbers of CD8⁺
166 T cells, resulting in a skewed CD4⁺ to CD8⁺ T cell ratio relative to clusters 1 and 2. Since
167 most samples in cluster 3 were surgical lobectomies from patients in South Africa, this
168 profile could be related to disease severity, comorbidity, or mandatory pre-surgical
169 antimicrobial therapy. Given this result, we analyzed therapeutic resections with respect
170 to HIV status (Extended Data Fig. 3). While we observed a slight difference in the CD4⁺
171 to CD8⁺ T cell ratio (approximately two-fold decrease in HIV⁺ specimens, p = 0.026), we
172 found no material differences in immune cell frequencies that define these clusters. Taken
173 together, this comprehensive cell census reveals distinct types of granulomas that are
174 defined by immune cell frequency and associate with TB disease status.

175

176 [Spatial analysis of granulomas identifies organized protein expression patterns and](#)
177 [conserved cellular microenvironments](#)

178 In order to identify recurrent patterns of protein co-expression in TB granulomas,
179 we conducted a spatial enrichment analysis that quantified the degree of co-occurrence
180 between pairs of proteins relative to a null distribution (Extended Data Fig. 4a)¹⁹. Pairwise

181 enrichment scores for each protein pair were then used to construct an interaction
182 network that was subsequently analyzed using a community detection algorithm²⁹ (Fig.
183 2a). This analysis resulted in three spatial modules consistent with canonical granuloma
184 structures, including the myeloid core, lymphocytic cuff, and stromal compartment.
185 Intriguingly, these modules also revealed more granular, previously unknown features
186 linking cell function to spatial organization, such as the association of the lymphocytic cuff
187 with H3K9Ac and the myeloid core with IDO1 and PD-L1 (Fig. 2a).

188 These findings motivated us to examine how the local cellular neighborhood
189 relates to single cell function and granuloma structure. Therefore, we employed spatial
190 Latent Dirichlet Allocation (spatial-LDA)³⁰ to discover and assign cellular
191 microenvironments (MEs) to each cell in a CPM, where an ME is defined by a set of cell
192 types found to be spatially co-occurring across the cohort. Using this approach, we
193 identified eight MEs for summarizing the local frequency of cell subsets within a 50 μ m
194 radius of a target cell (Fig. 2b). We then labeled each cell with its highest probability ME
195 to generate a maximum probability ME map (MaxPM, Fig. 2c, Extended Data Fig. 4b).
196 Through this approach, granuloma composition and structure can be summarized with
197 two complementary and simplified spatial representations: a CPM and MaxPM where
198 cells are labeled either by cell type or by ME, respectively (Fig. 2c).

199 This allowed us to annotate well known features of granuloma histology in an
200 unbiased fashion, while also revealing previously unrecognized cellular niches (Fig. 2d,
201 e). For example, the large majority of granuloma macrophages and monocytes were
202 assigned to one of three myeloid MEs (ME_{Mcore1} , $ME_{IntMono}$, ME_{Mcore2}). While ME_{Mcore1} was
203 found to some degree across all specimen types, $ME_{IntMono}$ and ME_{Mcore2} were significantly
204 enriched in either extra-pulmonary diagnostic biopsies or therapeutic resections,
205 respectively (Fig. 2f, Extended Data Fig. 4d, e). ME_{Mcore1} exhibited the strongest
206 preference for the histologically defined granuloma core region (median frequency in core
207 = 99.1%, Extended Data Fig. 4c) and was predominated by CD11c⁺ CD11b⁺
208 macrophages (Fig. 2d, e). ME_{Mcore2} exhibited myeloid core preference to a lesser extent
209 and was enriched for CD14⁺ classical monocytes (median frequency in core = 60.9%,

210 Extended Data Fig. 4c). Lastly, $ME_{IntMono}$ exhibited low myeloid core preference and was
211 enriched for $CD14^+ CD16^+$ intermediate monocytes (Fig. 2d, e).

212 ME_{Lcuff} aligned with the second histologically defined microenvironment in the
213 granuloma, the lymphocytic cuff, and was comprised predominantly of $CD4^+$ and $CD8^+$ T
214 cells (Fig. 2d, e). ME_{TLS} is a second lymphoid ME that is B cell predominated with sparse
215 numbers of follicular helper T cells ($CD4^+ PD-1^+$), consistent with tertiary lymphoid
216 structures (TLS, confirmed by H&E in serial sections, Fig. 2e)³¹⁻³³. This ME was highly
217 abundant in FOVs that were B cell predominated from cell frequency cluster 2 (Fig. 2f,
218 Fig. 1e).

219 As previously demonstrated, some granulomas exhibited a fibrotic wound healing
220 response consisting of fibroblasts and $CD163^+$ M2-like macrophages (Fig. 1e). These
221 cells were found to co-localize within ME_{Fib} , where $CD36$, a fibroblast marker, and
222 collagen-1, a marker for fibrosis are expressed (Fig. 2d, e)³⁴. The last two MEs
223 represented less characterized cellular environments in TB infection. ME_{Vasc} was
224 predominated by blood vessels and mast cells while ME_{Epi} was comprised of parenchymal
225 epithelial cells and $CD206^+$ alveolar-like macrophages (Fig. 2d, e). Given that they are
226 known to participate in angiogenesis, tissue repair, and immune cell recruitment³⁵,
227 perivascular localization of mast cells in the granuloma could suggest their involvement
228 in some of these processes. On the other hand, since ME_{Vasc} was found to be lower in
229 extra-pulmonary biopsies (Fig. 2f, Extended Data Fig. 4e), this may reflect organ-specific
230 differences in vascularity and abundance of tissue resident mast cells.

231 We next sought to compare sample composition with respect to ME frequency.
232 Using a correlation-based approach, we found that five ME frequency clusters accounted
233 for 89% of variance (Fig. 2f, Extended Data Fig. 4f). Notably, two of these clusters were
234 comprised of samples from more than one cell frequency cluster (as defined in Fig. 1e).
235 These clusters, along with a Principle Component Analysis (PCA) of all samples based
236 on mean ME probability, further supported tissue site and clinical cohort-associated ME
237 profiles (Fig. 2f, Extended Data Fig. 4g). Altogether, this suggests that MEs capture
238 recurrent spatial features of granulomas that are not discernible by bulk cell composition
239 alone.

weighted, undirected network (edge weight is proportional to average z-score) with three communities (myeloid core = green, lymphocytic cuff = blue, non-immune/other = pink). **(b)** Conceptual overview of spatial-LDA. **(c)** Cell probability map (left), max probability map (right), and microenvironment (ME) probability for 8 MEs (middle, scaled 0 -1) for a pulmonary TB section. **(d)** Heatmap of ME preferences for all subsets (standardized mean ME loading) with hierarchical clustering (Euclidean distance, complete linkage) and mean normalized expression of functional markers (probability weighted mean) with columns hierarchically clustered (Euclidean distance, complete linkage). **(e)** Biological classification of microenvironments. **(f)** Frequency of all MEs per FOV. Heatmap columns are hierarchically clustered (Pearson correlation, complete linkage). Paired ROIs from the same patient annotated with a black bar. ME and cell composition clusters annotated below dendrogram. Cell cluster annotation is based on clusters in Fig. 1e.

240

241 Granuloma myeloid cells are characterized by spatially coordinated expression of IDO1 242 and PD-L1

243 Our microenvironment and spatial protein network modeling revealed that myeloid-
244 rich regions in the granuloma are characterized by expression of two proteins, IDO1 and
245 PD-L1 (Fig. 2a, d). Given the tolerogenic role of these proteins^{36–41}, we sought to identify
246 myeloid cell subsets that could promote bacterial persistence through upregulation of
247 these pathways. We identified nine unique macrophage, monocyte, and dendritic cell
248 populations (Extended Data Fig. 2b, Fig. 3a). PD-L1 and IDO1 were correlated (Pearson
249 $R = 0.64$, $p < 2.2 \times 10^{-16}$) and expressed to varying degrees across most of these
250 populations and all FOVs (Fig. 3b-e, Extended Data Fig. 5a, c). Bright co-expression of
251 both proteins was observed in CD11b⁺ CD11c⁺ macrophages, consistent with an MDSC-
252 like phenotype⁴² (Fig. 3d). This was also found in CD209⁺ DCs and CD16⁺ CD14⁺
253 intermediate monocytes, where it was associated with HLA-DR downregulation (Fig. 3a-
254 d). While the frequency of IDO1⁺ cells did not vary significantly between tissue or
255 specimen type (Extended Data Fig. 5b), PD-L1⁺ cells were significantly higher in
256 diagnostic biopsies relative to therapeutic resections, with a notable enrichment in
257 extrapulmonary tissues (Extended Data Fig. 5b). Notably, neutrophils were also found to
258 express IDO1 or PD-L1 (Extended Data Fig. 5d). Given that they have been shown to
259 secrete anti-inflammatory cytokines in TB granulomas⁴³, these findings are consistent
260 with a regulatory effector function. Lastly, nearly 100% of multinucleated giant cells
261 expressed IDO1 and ~75% express PD-L1 (Fig. 3f).

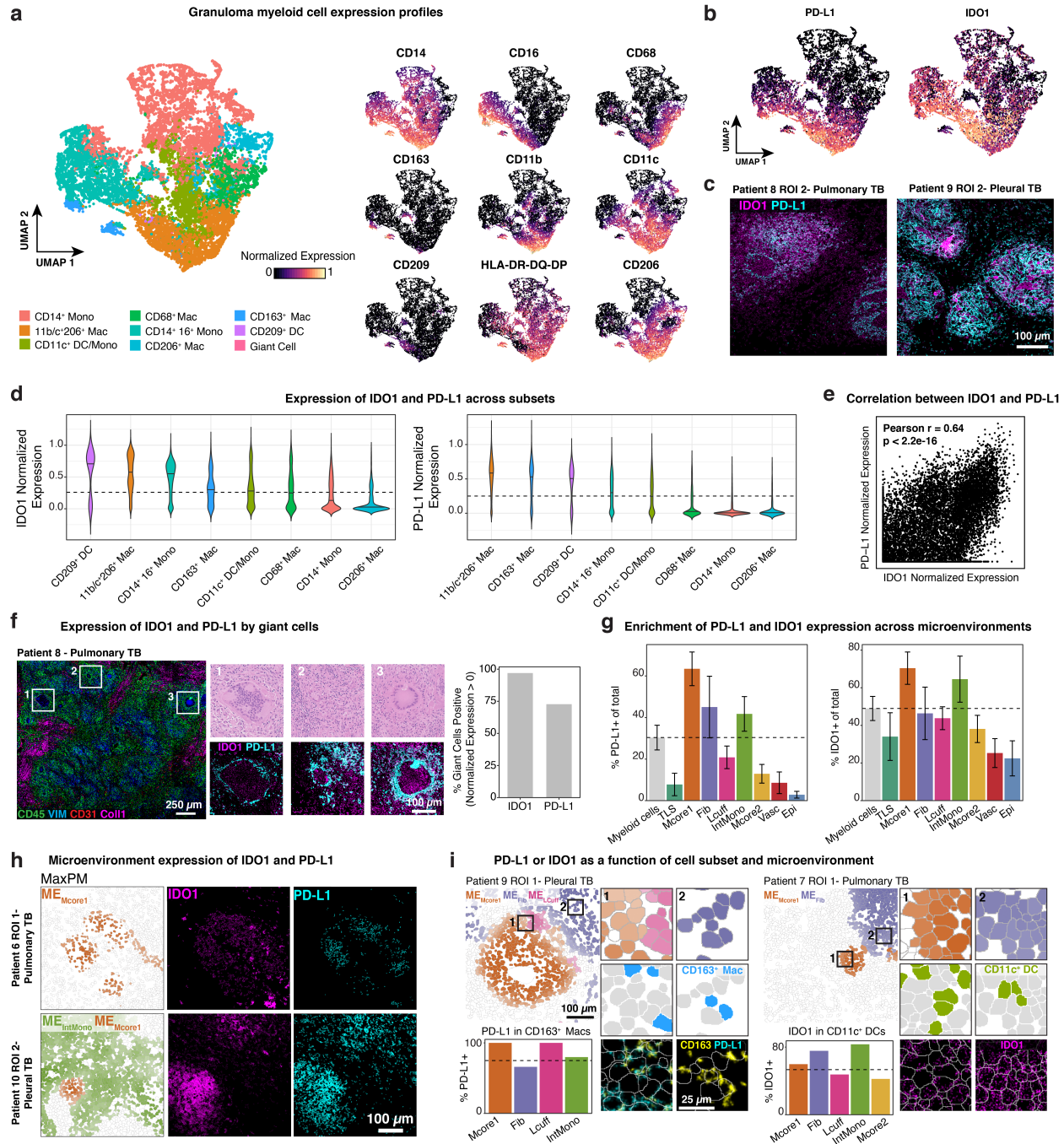


Figure 3. TB granuloma myeloid cells are characterized by spatially coordinated expression of IDO1 and PD-L1. (a) UMAP visualization of all myeloid populations across all TB FOVs colored by subset (left) and normalized expression of phenotypic markers used to delineate subsets. (b) IDO1 and PD-L1 normalized expression overlaid on the UMAP. (c) Representative images of a pulmonary (left) and pleural (right) sample showing expression of IDO1 (magenta) and PD-L1 (cyan). (d) Normalized expression of IDO1 (top) and PD-L1 (bottom) for major myeloid subsets ordered by decreasing median expression value. Dashed line indicates the cutoff for positivity for IDO1 (cutoff = 0.26) and PD-L1 (cutoff = 0.25). (e) PD-L1 and IDO1 expression values across all myeloid cells as a biaxial scatter plot. Plot displays Pearson's r and p -value determined by t-test. (f) Giant cells identified from a MIBI-scanned pulmonary TB sample (CD45 = green, Vimentin = blue, CD31 = red). Representative giant cells displayed in zoomed insets (lower left) with hematoxylin and eosin staining or IDO1 (magenta) and PD-L1 (cyan) expression. Bar plot displays the percentage of IDO1⁺ and PD-L1⁺ giant cells ($n = 33$, normalized expression > 0). (g) ME_{McCore1} and ME_{intMono} max

probability maps and representative images of a pulmonary (top) and pleural (bottom) TB sample showing expression of IDO1 (magenta) and PD-L1 (cyan). **(h)** The frequency of IDO1⁺ and PD-L1⁺ myeloid cells for all myeloid cells in aggregate and broken down by microenvironment. **(i)** The frequency of PD-L1⁺ CD163⁺ macrophages (left) across MEs with a representative MaxPM. Insets are colored by ME (top), cell type (blue, middle), and CD163 (yellow) and PD-L1 (cyan) with the segmentation boundaries overlaid (white). The frequency of IDO1⁺ CD11b⁺ CD11c⁺ macrophages (right) across MEs with a representative MaxPM. Insets are colored by ME (top), cell type (green, middle), and IDO1 (magenta) with the segmentation boundaries overlaid (white).

262

263 To determine how PD-L1 and IDO1 expression is associated with a cell's location
264 in the granuloma, we calculated the frequency of PD-L1⁺ and IDO1⁺ cells for each cell
265 subset in each ME (Fig. 3i, Extended Data Fig. 5e). We found that the majority of cells
266 displayed preferential, ME-specific expression patterns. For example, the frequency of
267 PD-L1 expressing CD163⁺ macrophages was highest in the ME_{Mcore1} (100%) and ME_{Lcuff}
268 (100%), while IDO1 expressing CD11b⁺ CD11c⁺ macrophages were most enriched in
269 ME_{Fib} (75.6%) and ME_{IntMono} (83.3%) (Fig. 3i). Altogether, PD-L1 and IDO1 expression
270 defines a newly identified, spatially-coordinated immunoregulatory feature of TB
271 granulomas that supports the possibility of highly localized, myeloid-mediated immune
272 suppression in the granuloma.

273

274 [Granuloma lymphocytes are enriched in distinct cellular microenvironments and display](#)
275 [a paradoxical absence of exhaustion markers](#)

276 We next wanted to assess if the spatial coordination observed in tolerogenic
277 myeloid cells extended to tolerogenic lymphocytes, like regulatory T cells (Tregs), which
278 comprised 1.3% of all lymphocytes (Fig. 4a). Tregs (CD3⁺ CD4⁺ Foxp3⁺) were
279 preferentially enriched in ME_{Mcore1} relative to ME_{Lcuff} (Fig. 4b, $p = 0.0012$), which stood in
280 contrast to all other lymphocyte subsets, including Foxp3⁻ CD4⁺ T cells. Furthermore, the
281 frequency of proliferating Tregs exceeded that of all other major lymphocyte subsets (Fig.
282 4c, $p < 0.001$). These results suggest that Tregs and MDSC-like cells preferentially
283 colocalize within ME_{Mcore1} to potentiate an immunomodulatory niche that could ultimately
284 deter bacterial clearance (Fig. 4d)^{44–50}.

285 Anti-inflammatory pathways like those found in ME_{Mcore1} are often induced as a
286 form of negative feedback that moderates the cytotoxic effects of unchecked immune
287 activation⁵¹. In line with this, high expression of PD-L1 and IDO1 by granuloma myeloid

288 cells would be expected to be accompanied by evidence of T cell activation in the form of
 289 checkpoint marker expression (e.g. PD-1, Lag3)⁵². For example, in previous work
 290 examining infiltrated triple negative breast cancer (TNBC) tumors, we found the median
 291 ratio of PD-1⁺: PD-L1⁺ immune cells to be near unity (Fig. 4f) and the prevalence of Lag3
 292 or PD-1 positive lymphocytes to be 13.9% and 5.5% on average, respectively (Fig. 4e).
 293 In contrast, PD-L1⁺ granuloma myeloid cells far outnumbered PD-1⁺ lymphocytes
 294 ($\log_2[\text{PD-1}^+ : \text{PD-L1}^+] = -5.73 \pm 3.4$, Fig. 4f). Furthermore, the small numbers of PD-1⁺
 295 lymphocytes in our dataset were almost entirely restricted to ME_{TLs}, consistent with T
 296 follicular helper cells rather than an activated or exhausted phenotype (Extended Data
 297 Fig. 5f). These findings are consistent with reports from the cynomolgus macaque model
 298 that also found low levels of PD-1, Lag3, and CTLA4¹⁴, suggesting that PD-L1 expression
 299 by myeloid granuloma cells occurs independently of local cytokine release by activated T
 300 cells.
 301

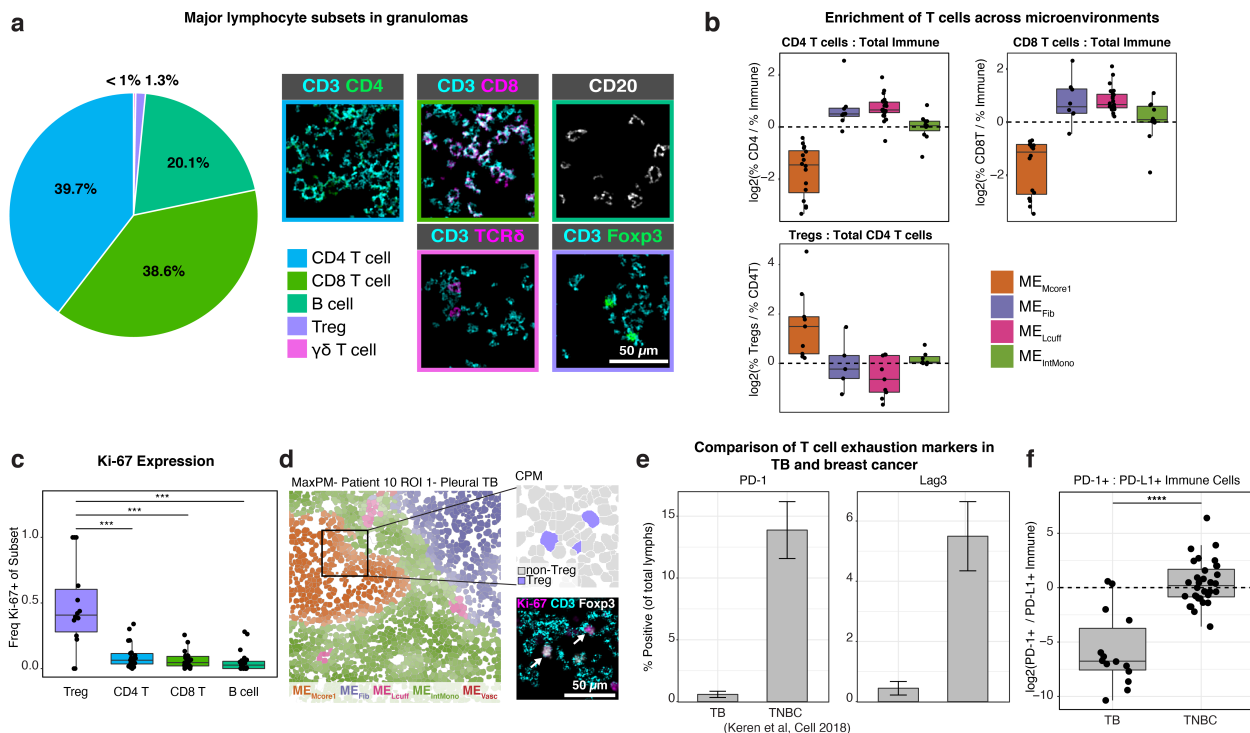


Figure 4. Granuloma lymphocytes are enriched in distinct cellular microenvironments and display a paradoxical absence of exhaustion markers. (a) Frequency of lymphocyte subsets in all TB FOVs pooled together (left) and representative images of each subset (right). (b) The frequency of CD4⁺ and CD8⁺ T cells relative to the frequency of total immune cells in four MEs of interest (top). The frequency of Tregs relative to the frequency of total CD4⁺ T cells (lower, left). (c) Frequency of Ki-67⁺ cells broken down by lymphocyte subset. (d) Representative image

from a pleural TB FOV, colored by ME assignment (left). Zoomed inset displays Treg assignment (upper-right, purple = Treg, grey = non-Treg) and expression of Ki-67 (magenta), CD3 (cyan), and Foxp3 (white) (lower-right). **(e)** Percent of lymphocytes positive for PD-1 (left) and Lag3 (right) in all TB FOVs and TNBC. Bar represents the mean and standard error. **(f)** The ratio of PD-1⁺: PD-L1⁺ immune cells represented as a log₂ fold-change in all TB FOVs and TNBC. All boxplots represent the median and interquartile range. All p-values determined with a Wilcoxon Rank Sum Test where: ns p > 0.05, * p < 0.05, ** p < 0.01, *** p < 0.001, **** p < 0.0001.

302

303 TB and sarcoidosis granulomas have both common and diverging features of immune 304 regulation

305 In addition to being the histological hallmark of TB, granulomatous inflammation
306 can occur in response to a foreign body or in autoimmune disorders, such as
307 sarcoidosis⁵³. Interestingly, several gene expression studies that have attempted to
308 develop blood-based biomarkers for latent and active infection have struggled to
309 differentiate between TB and sarcoidosis^{54,55}. In order to determine to what extent the
310 features identified here overlap with other granulomatous diseases, we compared the TB
311 sample cohort to ten sarcoidosis cases (Extended Data Fig. 6a-b). TB lesions were more
312 variable in composition (p = 0.037, Extended Data Fig. 6d) and had significantly higher
313 frequencies of CD8⁺ T cells, neutrophils, intermediate monocytes, and giant cells (Fig.
314 5a, Extended Data Fig. 6b-c). Sarcoid granulomas were heavily CD4⁺ T cell-skewed,
315 even relative to the CD4-skewed TB granulomas in our dataset, consistent with reports
316 of the pathology being driven primarily by Th17 and Th1 T cells (Fig. 5b)⁵⁶⁻⁵⁸.

317 Like TB, sarcoid lesions were PD-1 and Lag3 depleted (Fig. 5c) despite high levels
318 of PD-L1⁺ myeloid cells (Fig. 5d, Extended Data Fig. 6e). However, unlike TB, IDO1
319 expression in sarcoid samples was almost entirely absent (Fig. 5d). Since we used a
320 conservative threshold for IDO1 and PD-L1 positivity, our analysis biased toward the
321 moderate to bright-expressing cells present in TB granulomas and control tissues.
322 Therefore, to more comprehensively evaluate the disease specificity of PD-L1 and IDO1,
323 we performed immunohistochemistry (IHC) for both proteins on a tissue microarray of
324 granulomas from sarcoidosis (n = 9), foreign body uptake (n = 4), endometriosis (n = 4),
325 and xanthomatosis (n = 3) (Extended Data Fig. 6f). We identified weak expression of
326 IDO1 in several sarcoidosis lesions along with bright expression of PD-L1 as observed
327 by MIBI-TOF (Extended Data Fig. 6f). However, IDO1⁺ and PD-L1⁺ cells were nearly
328 absent in all xanthomas and endometrial lesions and rare in foreign body granulomas.

329 Notably, we observed similarly high levels of IDO1 and PD-L1 in a pulmonary
 330 *Mycobacterium avium* granuloma (Extended Data Fig. 6g). This supports that while PD-
 331 L1 expression could be a broader feature of certain granulomatous conditions, bright co-
 332 expression of IDO1 and PD-L1 may be specific to mycobacterial granulomas.
 333

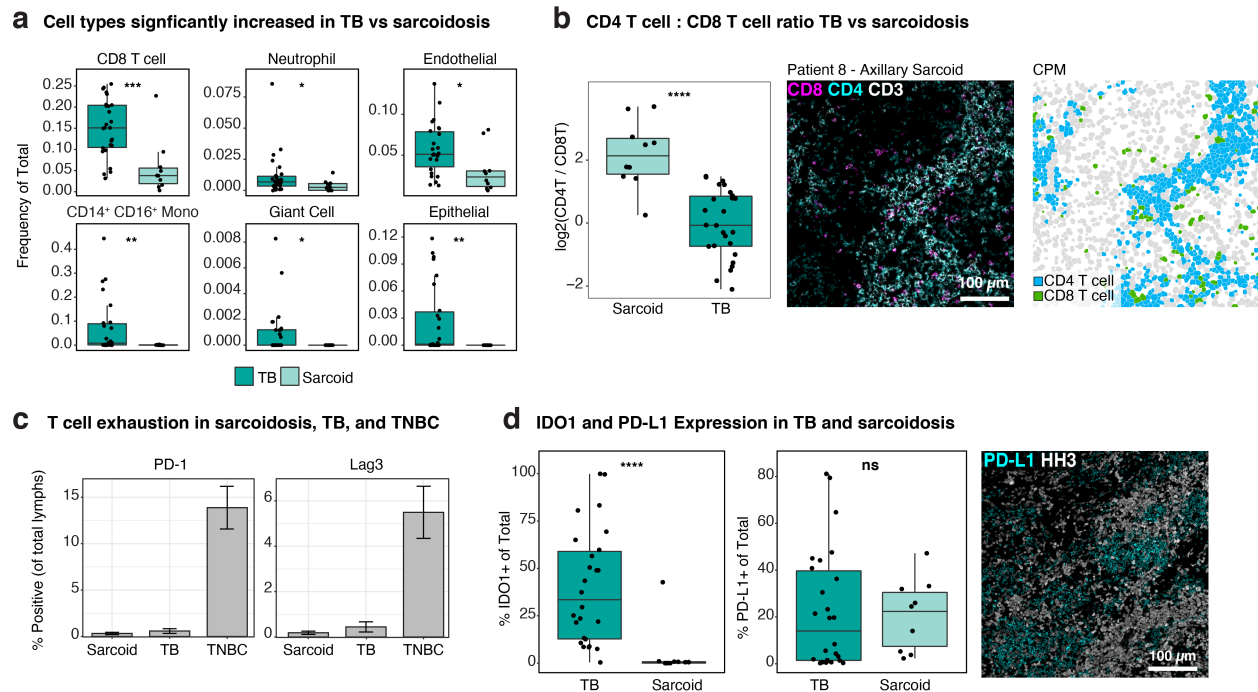


Figure 5. TB and sarcoidosis granulomas have both common and diverging features of immune regulation. (a) Frequency of cell subsets (of total cells) in TB versus sarcoidosis that are significantly different. **(b)** Comparison of the CD4⁺ T : CD8⁺ T cell ratio in TB versus sarcoidosis. Representative image of an axillary sarcoidosis FOV showing expression of CD8 (magenta), CD4 (cyan), and CD3 (white) (left) and colored by cell type (right, blue = CD4⁺ T cell, green = CD8⁺ T cell) **(c)** Percent of lymphocytes positive for PD-1 (left) and Lag3 (right) in all sarcoidosis FOVs, TB FOVs and TNBC. Bar represents the mean and standard error. **(d)** Percent of total cells positive for IDO1 or PD-L1 in TB and sarcoidosis. Representative image of a sarcoidosis FOV showing expression of PD-L1 (cyan) and HH3 (white). All boxplots represent the median and interquartile range. All p-values determined with a Wilcoxon Rank Sum Test where: ns p > 0.05, * p < 0.05, ** p < 0.01, *** p < 0.001, **** p < 0.0001.

334

335 [Immunoregulatory features of granulomas are reflected in the peripheral blood of TB](#)
 336 [patients where they correlate to clinical progression and treatment status](#)

337 The presence of immunosuppressive features in TB granulomas observed in our
 338 MIBI-TOF study has important implications for the treatment of TB infection. However,
 339 the invasive nature of procuring solid tissue limited the cohort size and scope by biasing
 340 towards advanced infections. Moreover, the single time point per patient in our tissue

341 dataset precludes temporal analysis that would correlate disease severity with granuloma
 342 immunosuppressive features. Given the clinical feasibility of venous phlebotomy and
 343 large number of publicly available blood transcriptomic datasets, we sought to correlate
 344 these features in blood from TB patients. Therefore, we used MetaIntegrator to perform
 345 several multi-cohort analyses using peripheral blood transcriptome profiles from healthy
 346 subjects and patients with latent or active TB infection^{59,60}.
 347

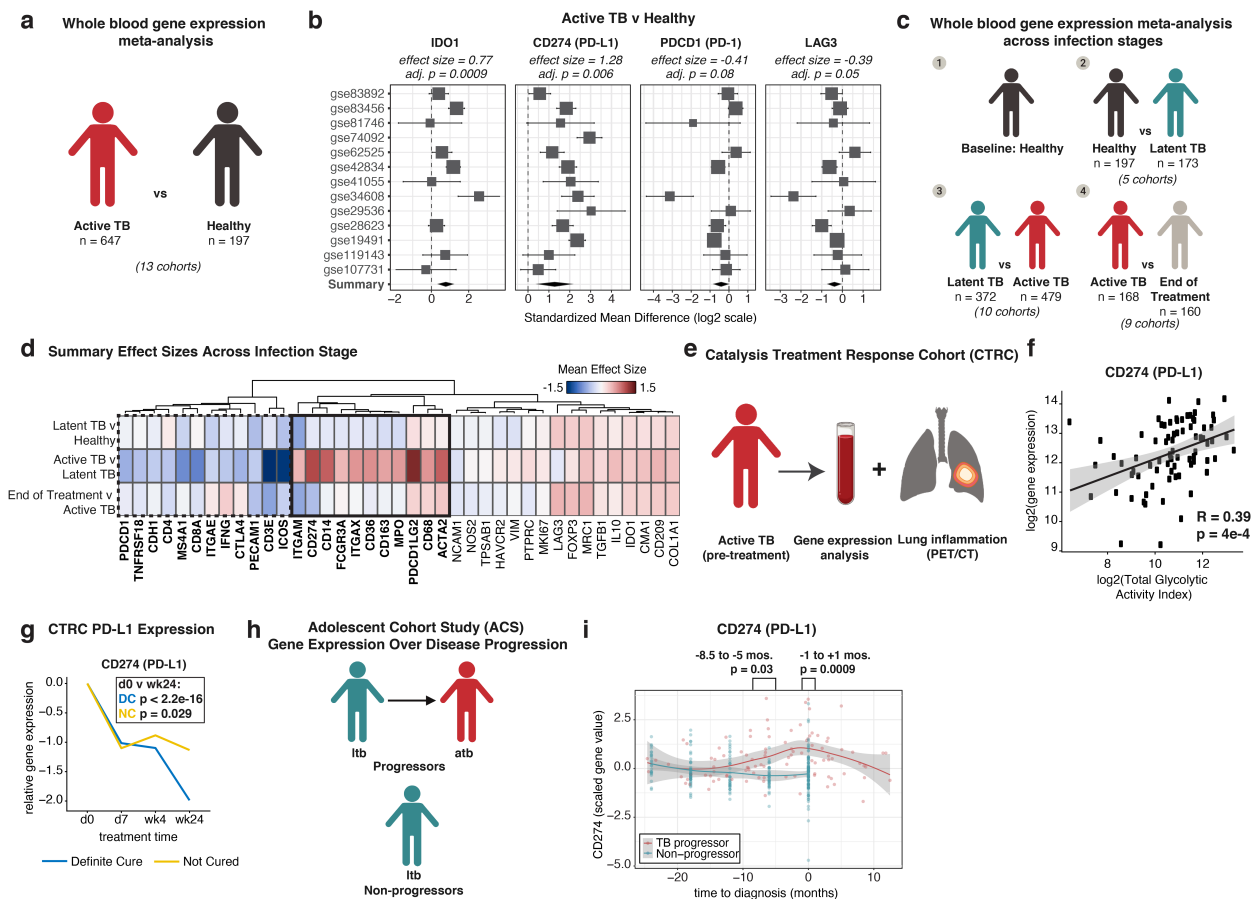


Figure 6. Immunoregulatory features of granulomas are reflected in the peripheral blood of TB patients where they correlate to clinical progression and treatment status (a) Conceptual overview of the meta-analysis of patients with active TB (n = 647) versus healthy controls (n = 197). **(b)** Forest plots of gene expression differences in active TB versus healthy individuals. Cohort identifiers are shown on the y-axis. Boxes represent the standardized mean difference in gene expression (effect size). The size of the box is proportional to the sample size of that cohort. Whiskers represent the 95% confidence interval and diamonds (black) represent the overall difference in gene expression between two groups by integrating the standardized mean differences across all cohorts. The width of the diamond corresponds to its 95% confidence interval. The adj. p values (*q* values, FDR 5%) for the summary effect sizes are shown above each plot. **(c)** Conceptual overview of gene expression analysis across clinical infection stage. **(d)** Heatmap of summary gene expression (mean effect size) values in latent TB (n = 173) versus healthy controls (n = 197), latent TB (n = 372) versus active TB (n = 479), and active TB (n = 168) versus end-of-treatment (n = 160). Clinical stage is displayed on rows and genes are displayed across columns hierarchically clustered (Euclidean distance, complete linkage). Genes upregulated in active TB versus latent TB are shown in the solid black box, while

downregulated genes are in the dashed black box. **(e)** Conceptual overview of the Catalysis Treatment Response Cohort (CTRC). **(f)** Correlation between PD-L1 gene expression and total glycolytic activity index (TGAi) represented as log₂-transformed values. Linear fit (blue) with 95% confidence interval (grey) displayed. A Pearson correlation of 0.39 ($p = 4 \times 10^{-4}$ t-test) is displayed below the linear fit. **(g)** PD-L1 gene expression across treatment time broken down by cure status (blue = definite cure and yellow = no cure). Line represents mean expression in each time point, connected across time points. P-value determined with Student's T-test for PD-L1 expression at d0 versus wk24 in the definite cure (DC, $n = 71$) and not-cured (NC, $n = 7$) groups. **(h)** Conceptual overview of the Adolescent Cohort Study (ACS). **(i)** PD-L1 gene expression in the ACS cohort across time prior to and after diagnosis of active TB stratified by progressors (red, $n = 34$) and non-progressors (blue, $n = 109$). Grey silhouette represents the 95% confidence interval. P-values determined by Welch two sample t-test.

348

349 We first determined if immune regulatory features identified in granulomas could
350 be detected in blood by comparing publicly available gene expression data of patients
351 with active TB ($n = 647$) to healthy controls ($n = 197$) from 13 independent cohorts (Fig.
352 6a). In line with PD-L1 and IDO1 expression in tissue data, significant and consistent
353 upregulation of *IDO1* and *CD274* (PD-L1) was found in patients with active TB infection
354 (effect size = 0.77 and 1.28, adj. $p = 0.0009$ and 0.006, respectively) (Fig. 6b).
355 Additionally, checkpoint depletion in lymphoid cells was corroborated as well, with
356 reduced expression of *PDCD1* (PD-1) and *LAG3* observed in the blood of active TB
357 patients (effect size = -0.41 and -0.39, adj. $p = 0.09$ and 0.05 respectively).

358 Next, we analyzed transcriptomic data from 1,549 patients across 24 cohorts in order
359 to determine if these features were specific to active infections. In line with the solid tissue
360 analysis, differential expression of genes associated with regulatory myeloid cells (e.g.
361 PDL1, PDL2, CD11b, CD11c, CD163) or T-cell immune checkpoint (e.g. PD1, CTLA4)
362 delineated active from latent infections (Fig. 6d). Moreover, the majority of these genes
363 returned to baseline levels seen in healthy controls after completing antimicrobial therapy
364 (Fig. 6d, Extended Data Fig. 6h). Taken together, these results suggest a shift toward
365 myeloid-mediated immune suppression that is specifically manifested during active TB
366 infection.

367 Because PD-L1 gene expression exhibited the largest effect size relative to healthy
368 controls, we next analyzed the Catalysis Treatment Response Cohort (CTRC) to
369 determine if PD-L1 could be used as a biomarker for estimating disease burden and
370 predicting clearance of infection (Fig 6e). Patients enrolled in this study provided venous
371 blood and underwent PET/CT imaging^{61,62}. Expression of PD-L1 at diagnosis was found
372 to be directly correlated with total glycolytic activity index (TGAi), a radiographic metric

373 for quantifying lung inflammation (Fig. 6f, Pearson $r = 0.39$ $p = 4 \times 10^{-4}$). 24 weeks after
374 treatment, patients were clinically classified into four groups: definite cure, probable cure,
375 possible cure, and not cured. Relative to the time of diagnosis, the reduction in PD-L1
376 expression in definitely cured patients ($n = 71$) were 2 times greater on average than in
377 uncured patients ($n = 7$, Fig. 6g). A nearly identical trend was observed for PD-L2 as well
378 (*PDCDLG2*, Extended Data Fig. 6i).

379 Lastly, we analyzed the Adolescent Cohort Study (ACS) to determine if PD-L1 could
380 be used for predicting progression to active disease. Latently infected individuals enrolled
381 in this study underwent regular blood collection and were clinically monitored for
382 symptoms of active infection (Fig. 6h)^{63,64}. PD-L1 transcript levels were significantly
383 elevated in progressors ($n = 34$) relative to non-progressors ($n = 109$) 8.5 months prior to
384 progression ($p = 0.03$) with the peak occurring at time of diagnosis ($p = 0.0009$) (Fig. 6i).
385 Taken together, these results raise the intriguing possibility for using PD-L1 expression
386 in peripheral blood as a predictive biomarker for early intervention in latently infected
387 individuals.

388

389 Discussion

390 After nearly 140 years of research into the pathophysiology of human TB infection,
391 central questions remain unresolved, in large part because granuloma formation and
392 progression are very difficult to emulate in tractable animal models. One of the most
393 critical questions that remains unanswered is which immune mechanisms drive
394 progression from latent infection to symptomatic active TB disease, the source of 11
395 million new cases and 1.5 million fatalities each year¹. Furthermore, individual granuloma
396 fate can vary significantly between lesions within individuals, raising questions about the
397 local immune dynamics that influence a granuloma's capacity to control infection while
398 mitigating tissue damage. With this in mind we used MIBI-TOF to identify recurrent
399 features of immune regulation in archival tissue from patients with active TB infection.
400 This spatial cell atlas allowed us to relate granuloma structure and composition. We
401 identified 19 unique cell subsets that preferentially organize into eight reoccurring cellular
402 microenvironments. TB granulomas appear to follow a consistent structural outline

403 characterized by spatially coordinated expression of PD-L1 and IDO1, myeloid core-
404 infiltrating Tregs, and a striking absence of T cell activation as measured through PD-1
405 and Lag3. Some of these features, such as high expression of PD-L1 and presence of
406 MDSC-like macrophages, were present in non-infectious granulomas as well pointing to
407 certain universal immune programs associated with the granulomatous immune
408 response. However, even compared to sarcoidosis, foreign body uptake, xanthomatosis,
409 and endometrial lesions, spatially coordinated expression of IDO1 and PD-L1 was unique
410 to mycobacterial granulomas.

411 Previous studies in the cynomolgus macaque model of TB have demonstrated that
412 granulomas from a single individual can have disparate outcomes with respect to bacterial
413 burden and inflammatory trajectory^{10,11}. The variation we see in our imaging dataset
414 suggests these local outcomes may be driven in part by unique cellular infiltrate and
415 structure within each granuloma. We observed that certain features, such as a high
416 frequency of CD8⁺ T cells, corresponded with reduced levels of more differentiated
417 macrophage phenotypes, a profile consistently present in therapeutic resections where
418 PD-L1 expression was also diminished. Since CD8⁺ T cells have been shown to be
419 critical for clearance of TB infection^{65,66}, understanding the immunological environments
420 that promote CD8⁺ T cell activity could reveal novel insights into immune features critical
421 for bacterial clearance.

422 By leveraging 29 publicly-available gene expression studies of over 1500 TB
423 patients and healthy controls, we were able to identify these immunoregulatory signatures
424 in peripheral blood and correlate them with disease burden and clinical outcome. Genes
425 found in solid tissue to be overexpressed at the protein level by immunosuppressive
426 myeloid cells (PD-L1, IDO1, CD163) were upregulated in blood. Similarly, genes
427 associated with T-cell activation were downregulated, consistent with the rare incidence
428 of PD-1 or Lag3 expression in tissue. Importantly, the magnitude of these trends was
429 distinctly higher in patients with active disease relative to those with latent or treated
430 infections. The highest effect size of genes measured in our analysis was observed for
431 PD-L1. PD-L1 was found to correlate with pulmonary disease burden and appears to be
432 a prognostic biomarker of progression from latent to active TB disease. Taken together,

433 the work presented here reveals new aspects of immune regulation in TB infection that
434 have important implications for understanding disease pathogenesis and improving
435 clinical management.

436 The high levels of PD-L1 and IDO1 observed in the near absence of PD-1 offers
437 clues into how the immunosuppressive niche during human infection is initiated and
438 maintained. These findings are consistent with a TGF β or IL-10 driven process where
439 production of these cytokines can suppress inflammation, promote immunosuppression,
440 and induce peripheral regulatory T cell differentiation and proliferation^{67–70}. This is
441 supported by recent work in mice where focal secretion of TGF- β within the myeloid core
442 was suggested to preferentially suppress neighboring T cells and in non-human primates
443 where granuloma formation was associated with IL-10 secretion^{71,72}.

444 Both IDO1 and PD-L1 have been shown to dampen anti-tumor immune responses
445 in cancer, which has prompted the development of host-directed immunotherapies⁷³. Our
446 findings suggest that similar approaches could be used to block PD-L1 mediated immune
447 suppression to promote bacterial clearance. However, evidence of T-cell activation or
448 exhaustion is not present in our dataset or in the cynomolgus macaque model. This
449 suggests that unlike checkpoint blockade in the setting of cancer, the efficacy of PD-L1
450 or PD-1 blockade could differ significantly. Recent reports of TB reactivation following PD-
451 1 blockade illustrate the seemingly paradoxical effects that can occur with host directed
452 therapies and emphasize the need to comprehensively map the temporal and spatial
453 dynamics of these pathways^{74–76}. In line with this, a critical next step will be to extend this
454 work to relate these features to bacterial burden, inflammatory dynamics, and granuloma
455 age in a primate model that accurately recapitulates human TB pathology.

456 To the best of our knowledge, this is the most comprehensive systems analysis of
457 TB to date. We identified dynamics of cellular composition and immunoregulatory
458 pathways in TB granulomas that are reflected in the peripheral immune response to TB.
459 These results have implications both for developing host-directed immunotherapies and
460 for identifying patients at risk of progression to active disease or treatment failure.
461 Expression of proteins such as IDO1 and PD-L1 aligns with immune evasion mechanisms
462 observed in tumor-immune microenvironment. The interface of granuloma and tumor

463 immunobiology offers vast opportunities to explore how tactics of immune evasion in
464 tumors may contribute to bacterial persistence in granulomas. Future multiplexed
465 imaging studies of granulomas from controlled TB exposures will offer novel insights on
466 how these local regulatory dynamics influence granuloma fate, and ultimately, infection
467 outcome.

468

469 **Data and Code Availability**

470 All custom code used to analyze data can be accessed at the following link:
471 <https://github.com/efrancis28/TBMIBI>. All processed images and annotated single cell
472 data will be made available on Mendeley Data.

473

474 **Methods**

475

476 ***Human Samples***

477 Human samples were acquired in accordance with IRB protocol # 46646.

478

479 ***Tuberculosis Granuloma Cohort***

480 Formalin-fixed Paraffin-embedded (FFPE) *Mtb* infected tissues were acquired from
481 Stanford Health Care's tissue repository from seven patients undergoing a pre-treatment
482 diagnostic biopsy. Tissues were screened to include those that were positive for Acid-
483 Fast Bacillus (AFB+) and *Mtb* DNA by polymerase chain reaction (PCR). Archival surgical
484 resection tissues were acquired from University of KwaZulu-Natal, Inkosi Albert Luthuli
485 Central Hospital from six patients with *Mtb* infection who underwent therapeutic resection
486 of infected tissue due to infection severity or treatment failure. This specimen group
487 contained HIV⁺ patients on antiretroviral therapy (n = 3), HIV⁻ patients (n = 2), and one
488 patient with no HIV infection reported. All clinical details for specimens can be found in
489 Extended Data Table 1. 5 μ m serial sections of each specimen were stained with
490 hematoxylin and eosin (H&E) and inspected by an anatomic pathologist to screen for the
491 presence of granulomatous inflammation. Regions with histologically solid granulomas or
492 cellular granulomatous inflammation were included. Regions with excessive fibrosis or

493 necrosis were excluded. Two 500 μm^2 fields of view (FOV) were chosen from each tissue
494 block for imaging.

495

496 ***Non-tuberculous Granulomas and Controls Tissues***

497 Regions of granulomatous inflammation from FFPE sarcoidosis and foreign body
498 reactions from Stanford Health Care were chosen by an anatomic pathologist. 0.5 mm
499 cores were selected and constructed into a tissue microarray (TMA). A pulmonary
500 *Mycobacterium avium* case was acquired from Stanford Health Care through selection
501 criteria of positive Acid-Fast Bacillus (AFB+) staining and PCR positivity for *M. avium*
502 *Complex* (MAC). A 5 μm serial section of this specimen was stained with hematoxylin and
503 eosin (H&E) and inspected by an anatomic pathologist to screen for the presence of
504 granulomatous inflammation. Control tissues of FFPE tonsil, spleen, and placenta were
505 acquired from Stanford Health Care. Small regions of each tissue were selected and
506 placed in a TMA.

507

508 ***Antibody Preparation***

509 Antibodies were conjugated to isotopic metal reporters as described previously¹⁹.
510 Following conjugation antibodies were diluted in Candor PBS Antibody Stabilization
511 solution (Candor Bioscience). Antibodies were either stored at 4°C or lyophilized in 100
512 mM D-(+)-Trehalose dehydrate (Sigma Aldrich) with ultrapure distilled H₂O for storage at
513 -20°C. Prior to staining, lyophilized antibodies were reconstituted in a buffer of Tris
514 (Thermo Fisher Scientific), sodium azide (Sigma Aldrich), ultrapure water (Thermo Fisher
515 Scientific), and antibody stabilizer (Candor Bioscienc) to a concentration of 0.05 mg/mL.
516 Information on the antibodies, metal reporters, and staining concentrations is located in
517 Extended Data Table 1.

518

519 ***Tissue Staining***

520 Tissues were sectioned (5 μm section thickness) from tissue blocks on gold and tantalum-
521 sputtered microscope slides. Slides were baked at 70 °C overnight followed by
522 deparaffinization and rehydration with washes in xylene (3x), 100% ethanol (2x), 95%

523 ethanol (2x), 80% ethanol (1x), 70% ethanol (1x), and ddH₂O with a Leica ST4020 Linear
524 Stainer (Leica Biosystems). Tissues next underwent antigen retrieval by submerging
525 sides in 3-in-1 Target Retrieval Solution (pH 9, DAKO Agilent) and incubating at 97 °C for
526 40 minutes in a Lab Vision PT Module (Thermo Fisher Scientific). After cooling to room
527 temperature slides were washed in 1x PBS IHC Washer Buffer with Tween 20 (Cell
528 Marque) with 0.1% (w/v) bovine serum albumin (Thermo Fisher). Next, all tissues
529 underwent two rounds of blocking, the first to block endogenous biotin and avidin with an
530 Avidin/Biotin Blocking Kit (Biolegend). Tissues were then washed with wash buffer and
531 blocked for 1 hour at room temperature with 1x TBS IHC Wash Buffer with Tween 20 with
532 3% (v/v) normal donkey serum (Sigma-Aldrich), 0.1% (v/v) cold fish skin gelatin (Sigma
533 Aldrich), 0.1% (v/v) Triton X-100, and 0.05% (v/v) Sodium Azide. The first antibody
534 cocktail was prepared in 1x TBS IHC Wash Buffer with Tween 20 with 3% (v/v) normal
535 donkey serum (Sigma-Aldrich) and filtered through a 0.1 µm centrifugal filter (Millipore)
536 prior to incubation with tissue overnight at 4 °C in a humidity chamber. Following the
537 overnight incubation slides were washed twice for 5 minutes in wash buffer. The second
538 day antibody cocktail was prepared as described and incubated with the tissues for 1
539 hour at 4 °C in a humidity chamber. Following staining, slides were washed twice for 5
540 minutes in wash buffer and fixed in a solution of 2% glutaraldehyde (Electron Microscopy
541 Sciences) solution in low-barium PBS for 5 minutes. Slides were washed in PBS (1x), 0.1
542 M Tris at pH 8.5 (3x), ddH₂O (2x), and then dehydrated by washing in 70% ethanol (1x),
543 80% ethanol (1x), 95% ethanol (2x), and 100% ethanol (2x). Slides were dried under
544 vacuum prior to imaging.

545

546 ***MIBI-TOF Imaging***

547 Imaging was performed using a MIBI-TOF instrument with a Hyperion ion source. Xe⁺
548 primary ions were used to sequentially sputter pixels for a given FOV. The following
549 imaging parameters were used:

550

- 551 • Acquisition setting: 80 kHz

- 552 • Field size: 500 μm^2 (TB, *M. avium* and controls) or 450 μm^2 (sarcoidosis) at 1024
- 553 x 1024 pixels
- 554 • Dwell time: 4 ms
- 555 • Median gun current on tissue: 1.45 nA Xe⁺
- 556 • Ion dose: 3.38 nAmp hours / mm² for 500 μm^2 FOVs and 3.75 nAmp hours / mm²
- 557 for 450 μm^2

558

559 ***Low-level Image Processing***

560 Multiplexed image sets were extracted, slide background-subtracted, denoised, and
561 aggregate filtered as previously described¹⁹. All parameters for these steps can be found
562 in Extended Data Table 1. In addition to these processing steps, image compensation
563 was performed to account for signal spillover due to adducts and oxides for the following
564 interferences: Collagen-1 to IDO1 and Lag3, H3K9Ac to panCK and MPO, Chym/Tryp to
565 MPO, Ki67 to CD209, CD20 to CD16, CD16 to IFN γ , CD11c to IDO1, and HLA-DR-DQ-
566 DP to CD11b.

567

568 ***Single Cell Segmentation***

569 Nuclear segmentation was performed using an adapted version of the DeepCell^{19–21} CNN
570 architecture. Training data was generated from MIBI-TOF images of human melanoma
571 that were stained with HH3 to identify nuclei and Na⁺K⁺ATPase to identify the cell
572 membrane. Color overlays of these two channels were used to manually segment nuclei
573 in ImageJ. This generated training data with labels for the nuclear interior, nuclear border,
574 and non-nuclear background. Training data was generated for 5 images to train the
575 network architecture. Images were divided into overlapping crops of 64x64 pixels. Each
576 crop was randomly flipped, rotated, and sheared during training to further augment the
577 available data. Stochastic gradient descent was used to train the network, combined with
578 early stopping to prevent over-fitting. Following training all MIBI-TOF images from our
579 cohorts were provided as input to the network to predict the class of each pixel: nuclear
580 interior, nuclear border, or non-nuclear background. The nuclear interior probability map
581 for each image was thresholded and segmented as described previously¹⁹ followed by a

582 3-pixel radial expansion around each nucleus to define the cell object boundaries. A
583 correction was applied to FOVs that contained multinucleated giant cells (MGNs). First
584 each MGN was identified using a combination of HH3, CD45, and Vimentin and manually
585 segmented in ImageJ to produce a binary mask of each MGN. All pixels within the binary
586 mask were reassigned to belong to the MGN cell object(s).

587

588 ***Single Cell Phenotyping and Composition***

589 Single cell data was extracted for all cell objects and area-normalized. Cells with a sum
590 of less than 0.1 area-normalized counts across all lineage channels were excluded from
591 analysis. Single cell data was linearly scaled with a scaling factor of 100 and asinh-
592 transformed with a co-factor of 5. All mass channels were scaled to 99.9th percentile. In
593 order to assign each cell to a lineage, the FlowSOM clustering algorithm was used in
594 iterative rounds with the Bioconductor “FlowSOM” package in R²². The first clustering
595 round separated cells into four major lineages using the “Metaclustering_consensus”
596 function: immune, epithelial, fibroblast, and endothelial. Immune cells were then clustered
597 again to delineate B cells, CD4⁺ T cells, CD8⁺ T cells, Tregs, neutrophils, mast cells, and
598 mononuclear phagocytes (macrophages, monocytes, and dendritic cells). Immune cells
599 with an expression profile not consistent with any of those subsets were annotated as
600 ‘other immune.’ Lastly, the mononuclear phagocytes were clustered to 25 metaclusters
601 which were merged into 7 groups. Giant cells were manually identified. $\gamma\delta$ T cells were
602 annotated as T cells with CD3 signal greater than or equal to the mean expression of
603 CD4⁺ T cells and TCR- δ signal > 0.5 normalized expression. CD163 macrophages were
604 identified as those with CD163 signal > 0.5 normalized expression. The relative
605 abundance of all major lineages was determined out of total cells per FOV and the relative
606 frequency of immune cell subsets was determined out of total immune cells per FOV.

607

608 ***Immune Cell Composition Clustering and Cell Type Association Analysis***

609 The Pearson correlation coefficient was calculated between all pairs of TB FOVs based
610 on the relative frequency of all immune cell subsets. The coefficients were used to
611 hierarchically cluster the FOVs using complete linkage and a distance metric of 1-

612 correlation coefficient. To identify consensus clusters the percent variance explained was
613 measured across a range of 1-10 clusters. The elbow point of this plot was used to
614 determine the optimal number of clusters. A randomized dataset was produced to
615 compare to the observed clustering by randomizing the frequency values across immune
616 cell subsets within each FOV. This dataset was also clustered using the Pearson
617 correlation coefficient and compared with the observed result. To assess the significance
618 of co-occurrence of cell types, a chi-square test was run between all cell type pairs using
619 the counts of each cell type across all TB FOVs. The resulting p-values were adjusted
620 using a false discovery rate (FDR) of 5%.

621

622 ***Protein Enrichment Analysis***

623 A spatial enrichment approach was used as previously described¹⁹ to identify patterns
624 of protein enrichment or exclusion across all protein pairs. HH3, Na⁺K⁺ATPase, and HLA
625 Class 1 were excluded from the analysis. For each pair of markers, X and Y, the number
626 of times cells positive for protein X was within a ~50 um radius of cells positive for protein
627 Y was counted. Thresholds for positivity were customized to each marker individually
628 using a silhouette scanning approach from the MetaCyto software in R⁷⁷. A null
629 distribution was produced by performing 1000 bootstrap permutations where the locations
630 of cells positive for protein Y were randomized. A z-score was calculated comparing the
631 number of true cooccurrences of cells positive for protein X and Y relative to the null
632 distribution. For each pair of proteins X and Y the average z-score was calculated across
633 all TB FOVs. Next, all positive enrichments between protein pairs (average Z score > 0,
634 excluded self-self protein enrichment scores) were used to produce a weighted,
635 undirected network where the nodes are the individual markers and the edge weights are
636 proportional to the average z-score (higher z-score → shorter edge length). The leading
637 eigenvector algorithm for community detection was used to identify protein enrichment
638 communities in this network⁷⁸.

639

640 ***Spatial Latent Dirichlet Allocation***

641 Spatial-LDA is an adaptation of Latent Dirichlet Allocation (LDA), a machine learning
642 approach used to model topics in text documents, where topics consist of words with a
643 high probability of cooccurrence, allowing mapping of topics to abstract definitions (ex.
644 ['dog', 'frog', 'horse'] → 'animals'). Spatial-LDA builds on this paradigm by representing
645 CPMs as documents and cell types as words. Spatial-LDA was conducted to identify
646 topics (here referred to as microenvironments) across all TB FOVs. Cell types with fewer
647 than 100 cells across the entire cohort were excluded from analysis ($\gamma\delta$ T cells and
648 CD209⁺ DC). Furthermore, multinucleated giant cells were excluded due to their cell size.
649 Spatial-LDA was implemented as described³⁰ with $d = 1000$, a spatial radius $r = 50 \mu\text{m}$
650 to complement the protein enrichment analysis, and a microenvironment (ME) number of
651 $n = 8$. The ME number was determined empirically. For each FOV a maximum probability
652 map (MaxPM) was produced by classifying each cell to the microenvironment with the
653 highest probability and coloring that cell by its microenvironment and probability. The cell
654 type preferences for each ME were determined by assessing the mean probability for all
655 cell types across all MEs. The mean expression for each functional marker across MEs
656 was determined by weighting protein expression by ME probability and calculating the
657 mean of weighted expression values across markers and MEs. The mean probability for
658 all MEs was determined for all FOVs (average of single cell values) and used to conduct
659 a Principal Component Analysis (PCA). The clustering approach described for immune
660 cell frequency clusters (above) was applied to ME frequencies across FOVs to identify
661 the optimal number of ME clusters to capture the maximal variance in our dataset.

662

663 ***Identification of the Myeloid Core***

664 In order to assess which microenvironments represented the histologically defined
665 myeloid core, binary masks of the myeloid core were generated for 18/26 FOVs. The
666 masks were generated by first combining the signal of CD11c, CD11b, CD14, CD206,
667 CD68, and PD-L1. The combined images were imported into ImageJ and hand-annotated
668 using ROI annotation tools. The annotated ROI was exported as a binary mask. This
669 mask was further processed in Matlab to close any holes, exclude objects smaller than
670 1000 pixels, and dilate the mask to smooth edges. Next cells were assigned to belonging

671 to the myeloid core if they had complete overlap with the binary mask. Cells on the mask
672 boundary or outside of the mask were designated as ‘non-myeloid core.’ The proportion
673 of cells in the myeloid core was assessed across each ME for the 18 FOVs and a MEs
674 with a median frequency in the myeloid core > 50% were designated as myeloid core
675 MEs.

676

677 ***Myeloid Cell UMAP Visualization***

678 UMAP embeddings were determined for all non-granulocytic myeloid cells using the R
679 implementation⁷⁹ with the following parameters: n_neighbors = 15, min_dist = 0.1 and
680 the following markers: CD45, CD68, CD206, CD11c, CD11b, CD14, CD16, CD209, and
681 CD163.

682

683 ***Immunoregulatory Protein Analysis***

684 Positivity thresholds for IDO1, PD-L1, PD-1, and Lag3 were automatically determined as
685 described above. Immune control tissues tonsil, spleen, and placenta were used to
686 validate antibody performance. Correlation between IDO1 and PD-L1 was determined
687 across the entire cohort and subsets of specimens using Pearson correlation analysis.
688 The frequency of cells positive for IDO1 and PD-L1 were enumerated across all subsets.
689 To assess PD-L1 and IDO1 positivity with respect to ME and cell subset, the total number
690 of cells across all myeloid subsets per ME was pooled across all FOVs. The quantity of
691 cells for each subset positive for IDO1 or PD-L1 was determined per ME. Any ME with <
692 1% of the total for a subset was excluded from analysis. PD-1 and Lag3 expression were
693 analyzed on lymphocytes or total immune cells. PD-1 and Lag3 were also analyzed on
694 immune cells from a human Triple Negative Breast Cancer (TNBC) cohort that was
695 previously published by our group¹⁹. Positivity for PD-1 and Lag3 for TNBC immune cells
696 was determined as described in the originally published study.

697

698 ***Cell Composition Analysis of Sarcoidosis and Tuberculosis***

699 Single cells from sarcoidosis FOVs were segmented as described above. Single cell data
700 was extracted, transformed, and normalized along with TB single cell data. Single cells

701 were included in the described FlowSOM clustering procedure. To compare the cellular
702 diversity of TB with sarcoidosis the Shannon Diversity Index was calculated using the
703 counts of all cell subsets per TB or sarcoidosis FOV.

704

705 ***Immunohistochemistry of PD-L1 and IDO1***

706 Immunohistochemistry (IHC) for PD-L1 and IDO1 was performed using the antibody
707 reagents in Extended Data Table 1 at a concentration of 1 $\mu\text{g}/\text{mL}$. The IHC protocol
708 mirrors the MIBI-TOF protocol with the addition of blocking endogenous peroxidase
709 activity with 3% H_2O_2 (Sigma Aldrich) in dd H_2O after epitope retrieval. On the second day
710 of staining, instead of proceeding with the MIBI-TOF protocol, tissues were washed twice
711 for 5 minutes in wash buffer and stained using the ImmPRESS universal (Anti-
712 Mouse/Anti-Rabbit) kit (Vector labs).

713

714 ***Whole Blood Transcriptomic Analysis***

715 Publicly available gene expression data sets (Extended Data Table 2) were collected,
716 annotated, and used for meta-analysis conducted using MetaIntegrator⁵⁹. Gene
717 expression matrices were prepared for each dataset to determine effect sizes for genes
718 of all proteins included in the MIBI-TOF analysis and an additional set of genes with
719 similar biological function, such as *ICOS* and *CTLA4*. Summary effect sizes were
720 calculated to assess gene expression differences across clinical groups (healthy, active
721 TB, latent TB, end of treatment, TB progression, and during treatment). For the Catalysis
722 Treatment Response Cohort (CTRC) gene expression measurements at diagnosis of TB
723 were correlated with matched Total Glycolytic Activity Index (TGAI), a readout of PET-CT
724 activity. A linear regression was fit between *CD274* gene expression and *TGAI* and the
725 correlation was assessed with Pearson correlation analysis. To assess *CD274* and
726 *PDCDLG2* gene expression over treatment, expression values were normalized to the
727 measurement taken at diagnosis (d0). Gene expression data in the Adolescent Cohort
728 Study (ACS) were separated by progression status. Local regression (LOESS) was used
729 to fit the gene expression data over time in each group. The significance of separation

730 between progressors and non-progressors was determined in two different time intervals
731 using a Student's t-test.

732

733 **Software**

734 Image processing was conducted with Matlab 2016a and Matlab 2019b. Statistical
735 analysis was conducted in Matlab 2016a, Matlab 2019b, and R. Data visualization and
736 plots were generated in R. Representative images were processed in Adobe Photoshop
737 and figures were prepared in Adobe Illustrator. Schematic visualizations were produced
738 with Biorender.

739

740 **Author Contributions:**

741 E.F.M conceived the study design, performed experiments, analyzed data, and wrote the
742 manuscript. M.D. conducted the blood transcriptomics analysis. L.K. assisted with
743 analysis conceptualization. Z.C. and V.J. implemented the spatial-LDA analysis. L.K,
744 A.D., N.F.G., A.B., and W.G. assisted with data analysis. M.B. assisted with assay
745 development. D.V.V. developed Deepcell. M.F., P.K.R., E.F., M.V.D.R., N.B., and
746 A.J.C.S. provided samples and consulted on tissue cohort design. S.C.B, P.K., and M.A.
747 supervised the work.

748

749 **Acknowledgments**

750 The authors thank Tyler Risom, David Glass, Matthew Carter, and Anne Kasmar for
751 discussions and comments. The authors thank Pauline Chu and the Stanford Human
752 Histology Core for providing technical assistance. E.F.M was supported by the NSF
753 Graduate Research Fellowship (grant no. 2017242837). L.K. was a Damon Runyon
754 Fellow supported by the Damon Runyon Cancer Research Foundation (DRG-2292-17)
755 and a non-stipendiary awardee of the EMBO Long-Term fellowship (ALTF 1128–2016).
756 Noah Greenwald was supported by F31CA246880. A.J.C.S. was supported
757 R61/33AI138280, R01AI134810, the CRDF Global, the South African Medical Research
758 Council, and an NRF BRICS Multilateral grant to A.J.C.S. M.A. was supported by 1-DP5-
759 OD019822. S.C.B. and M.A. were jointly supported by 1R01AG056287 and

760 1R01AG057915, 1U24CA224309, the Bill and Melinda Gates Foundation, and a
761 Translational Research Award from the Stanford Cancer Institute. S.J.G. was supported
762 by U19 AI104209, R01 AR067145, and R01 AI32494.

763

764 **Conflicts of Interest**

765 M.A. and S.C.B. are inventors on patent US20150287578A1. M.A. and S.C.B. are board
766 members and shareholders in IonPath Inc. E.F.M. has previously consulted for IonPath
767 Inc.

768

769 **References**

770

- 771 1. WHO | Global tuberculosis report 2019. *WHO* (2020).
- 772 2. Cohen, S. B. *et al.* Alveolar Macrophages Provide an Early Mycobacterium
773 tuberculosis Niche and Initiate Dissemination. *Cell Host Microbe* **24**, 439-446.e4
774 (2018).
- 775 3. Wolf, A. J. *et al.* Mycobacterium tuberculosis Infects Dendritic Cells with High
776 Frequency and Impairs Their Function In Vivo . *J. Immunol.* **179**, 2509–2519
777 (2007).
- 778 4. Bold, T. D. & Ernst, J. D. Who benefits from granulomas, mycobacteria or host?
779 *Cell* **136**, 17–9 (2009).
- 780 5. Davis, J. M. & Ramakrishnan, L. The Role of the Granuloma in Expansion and
781 Dissemination of Early Tuberculous Infection. *Cell* **136**, 37–49 (2009).
- 782 6. Ramakrishnan, L. Revisiting the role of the granuloma in tuberculosis. *Nat. Rev.*
783 *Immunol.* **12**, (2012).
- 784 7. Cadena, A. M., Fortune, S. M. & Flynn, J. L. Heterogeneity in tuberculosis. (2017)
785 doi:10.1038/nri.2017.69.
- 786 8. Subbian, S. *et al.* Lesion-Specific Immune Response in Granulomas of Patients
787 with Pulmonary Tuberculosis: A Pilot Study. *PLoS One* **10**, e0132249 (2015).
- 788 9. Coleman, M. T. *et al.* Early Changes by (18)Fluorodeoxyglucose positron
789 emission tomography coregistered with computed tomography predict outcome
790 after Mycobacterium tuberculosis infection in cynomolgus macaques. *Infect.*
791 *Immun.* **82**, 2400–4 (2014).
- 792 10. Lin, P. L. *et al.* Sterilization of granulomas is common in active and latent
793 tuberculosis despite within-host variability in bacterial killing. *Nat. Med.* **20**, 75–79
794 (2013).
- 795 11. Martin, C. J. *et al.* Digitally Barcoding Mycobacterium tuberculosis Reveals In Vivo
796 Infection Dynamics in the Macaque Model of Tuberculosis. *MBio* **8**, e00312-17
797 (2017).
- 798 12. Carow, B. *et al.* Spatial and temporal localization of immune transcripts defines
799 hallmarks and diversity in the tuberculosis granuloma. *Nat. Commun.* **10**, 1–15
800 (2019).

- 801 13. Marakalala, M. J. *et al.* Inflammatory signaling in human tuberculosis granulomas
802 is spatially organized. *Nat. Med.* **22**, 531–538 (2016).
- 803 14. Wong, E. A. *et al.* Low levels of T cell exhaustion in tuberculous lung granulomas.
804 *Infect. Immun.* **86**, (2018).
- 805 15. Kauffman, K. D. *et al.* Defective positioning in granulomas but not lung-homing
806 limits CD4 T-cell interactions with Mycobacterium tuberculosis-infected
807 macrophages in rhesus macaques. *Mucosal Immunol.* **11**, 462–473 (2018).
- 808 16. Keren, L. *et al.* MIBI-TOF: A multiplexed imaging platform relates cellular
809 phenotypes and tissue structure. *Sci. Adv.* **5**, eaax5851 (2019).
- 810 17. Krishnan, N., Robertson, B. D. & Thwaites, G. The mechanisms and
811 consequences of the extra-pulmonary dissemination of Mycobacterium
812 tuberculosis. *Tuberculosis* vol. 90 361–366 (2010).
- 813 18. Ranaivomanana, P. *et al.* Cytokine Biomarkers Associated with Human Extra-
814 Pulmonary Tuberculosis Clinical Strains and Symptoms. *Front. Microbiol.* **9**, 275
815 (2018).
- 816 19. Keren, L. *et al.* A Structured Tumor-Immune Microenvironment in Triple Negative
817 Breast Cancer Revealed by Multiplexed Ion Beam Imaging. *Cell* **174**, 1373-
818 1387.e19 (2018).
- 819 20. Van Valen, D. A. *et al.* Deep Learning Automates the Quantitative Analysis of
820 Individual Cells in Live-Cell Imaging Experiments. *PLOS Comput. Biol.* **12**,
821 e1005177 (2016).
- 822 21. Bannon, D. *et al.* Dynamic allocation of computational resources for deep
823 learning-enabled cellular image analysis with Kubernetes. *bioRxiv* 505032 (2019)
824 doi:10.1101/505032.
- 825 22. Van Gassen, S. *et al.* FlowSOM: Using self-organizing maps for visualization and
826 interpretation of cytometry data. *Cytom. Part A* **87**, 636–645 (2015).
- 827 23. Flynn, J. L., Chan, J. & Lin, P. L. Macrophages and control of granulomatous
828 inflammation in tuberculosis. *Mucosal Immunology* vol. 4 271–278 (2011).
- 829 24. Garcia-Rodriguez, K. M., Goenka, A., Alonso-Rasgado, M. T., Hernández-Pando,
830 R. & Bulfone-Paus, S. The role of mast cells in tuberculosis: Orchestrating innate
831 immune crosstalk? *Frontiers in Immunology* vol. 8 (2017).
- 832 25. Ratnam, S., Ratnam, S., Puri, B. K. & Chandrasekhar, S. Mast cell response
833 during the early phase of tuberculosis: an electron microscopic study. *Can. J.*
834 *Microbiol.* **23**, 1245–1251 (1977).
- 835 26. Carlos, D. *et al.* Mast Cells Modulate Pulmonary Acute Inflammation and Host
836 Defense in a Murine Model of Tuberculosis. *J. Infect. Dis.* **196**, 1361–1368 (2007).
- 837 27. Polena, H. *et al.* Mycobacterium tuberculosis exploits the formation of new blood
838 vessels for its dissemination. *Sci. Rep.* **6**, 1–11 (2016).
- 839 28. Oehlers, S. H. *et al.* Interception of host angiogenic signalling limits mycobacterial
840 growth. *Nature* **517**, 612–615 (2015).
- 841 29. Girvan, M. & Newman, M. E. J. Community structure in social and biological
842 networks. *Proc. Natl. Acad. Sci. U. S. A.* **99**, 7821–7826 (2002).
- 843 30. Chen, Z., Soifer, I., Hilton, H., Keren, L. & Jovic, V. Modeling Multiplexed Images
844 with Spatial-LDA Reveals Novel Tissue Microenvironments . *J. Comput. Biol.*

- 845 (2020) doi:10.1089/cmb.2019.0340.
- 846 31. Shi, J. *et al.* PD-1 Controls Follicular T Helper Cell Positioning and Function.
847 *Immunity* **49**, 264-274.e4 (2018).
- 848 32. Dieu-Nosjean, M. C., Goc, J., Giraldo, N. A., Sautès-Fridman, C. & Fridman, W.
849 H. Tertiary lymphoid structures in cancer and beyond. *Trends in Immunology* vol.
850 35 571–580 (2014).
- 851 33. Ulrichs, T. *et al.* Human tuberculous granulomas induce peripheral lymphoid
852 follicle-like structures to orchestrate local host defence in the lung. *J. Pathol.* **204**,
853 217–228 (2004).
- 854 34. Difazio, R. M. *et al.* Active transforming growth factor- β is associated with
855 phenotypic changes in granulomas after drug treatment in pulmonary
856 tuberculosis. *DARU, J. Pharm. Sci.* **24**, 6 (2016).
- 857 35. Krystel-Whittemore, M., Dileepan, K. N. & Wood, J. G. Mast cell: A multi-
858 functional master cell. *Frontiers in Immunology* vol. 6 (2016).
- 859 36. Shen, L. *et al.* PD-1/PD-L pathway inhibits M.tb-specific CD4+ T-cell functions
860 and phagocytosis of macrophages in active tuberculosis. *Sci. Rep.* **6**, 38362
861 (2016).
- 862 37. Shen, L. *et al.* The characteristic profiles of PD-1 and PD-L1 expressions and
863 dynamic changes during treatment in active tuberculosis. *Tuberculosis* **101**, 146–
864 150 (2016).
- 865 38. Mehra, S. *et al.* Granuloma correlates of protection against tuberculosis and
866 mechanisms of immune modulation by Mycobacterium tuberculosis. *J. Infect. Dis.*
867 **207**, 1115–27 (2013).
- 868 39. Munn, D. H. & Mellor, A. L. IDO in the Tumor Microenvironment: Inflammation,
869 Counter-Regulation, and Tolerance. *Trends in Immunology* vol. 37 193–207
870 (2016).
- 871 40. Gautam, U. S. *et al.* In vivo inhibition of tryptophan catabolism reorganizes the
872 tuberculoma and augments immune-mediated control of Mycobacterium
873 tuberculosis. *Proc. Natl. Acad. Sci. U. S. A.* **115**, E62–E71 (2018).
- 874 41. Jurado, J. O. *et al.* Programmed death (PD)-1:PD-ligand 1/PD-ligand 2 pathway
875 inhibits T cell effector functions during human tuberculosis. *J. Immunol.* **181**, 116–
876 25 (2008).
- 877 42. Human myeloid derived suppressor cell (MDSC) subset phenotypes | The Journal
878 of Immunology. https://www.jimmunol.org/content/198/1_Supplement/211.2.
- 879 43. Gideon, H. P., Phuah, J., Junecko, B. A. & Mattila, J. T. Neutrophils express pro-
880 and anti-inflammatory cytokines in granulomas from Mycobacterium tuberculosis-
881 infected cynomolgus macaques. *Mucosal Immunol.* **12**, 1370–1381 (2019).
- 882 44. Kanamori, M., Nakatsukasa, H., Okada, M., Lu, Q. & Yoshimura, A. Induced
883 Regulatory T Cells: Their Development, Stability, and Applications. *Trends in*
884 *Immunology* vol. 37 803–811 (2016).
- 885 45. Hsu, P. *et al.* IL-10 Potentiates Differentiation of Human Induced Regulatory T
886 Cells via STAT3 and Foxo1. *J. Immunol.* **195**, 3665–3674 (2015).
- 887 46. Llopiz, D. *et al.* IL-10 expression defines an immunosuppressive dendritic cell
888 population induced by antitumor therapeutic vaccination. *Oncotarget* **8**, 2659–

- 889 2671 (2017).
- 890 47. Ribeiro-Rodrigues, R. *et al.* A role for CD4+CD25+ T cells in regulation of the
891 immune response during human tuberculosis. *Clin. Exp. Immunol.* **144**, 25–34
892 (2006).
- 893 48. Scott-Browne, J. P. *et al.* Expansion and function of Foxp3-expressing T
894 regulatory cells during tuberculosis. *J. Exp. Med.* **204**, 2159–2169 (2007).
- 895 49. Guyot-Revol, V., Innes, J. A., Hackforth, S., Hinks, T. & Lalvani, A. Regulatory T
896 cells are expanded in blood and disease sites in patients with tuberculosis. *Am. J.*
897 *Respir. Crit. Care Med.* **173**, 803–810 (2006).
- 898 50. Green, A. M. *et al.* CD4 + Regulatory T Cells in a Cynomolgus Macaque Model of
899 Mycobacterium tuberculosis Infection . *J. Infect. Dis.* **202**, 533–541 (2010).
- 900 51. Bagaitkar, J. Cellular dynamics of resolving inflammation. *Blood* vol. 124 1701–
901 1703 (2014).
- 902 52. Wherry, E. J. & Kurachi, M. Molecular and cellular insights into T cell exhaustion.
903 *Nature Reviews Immunology* vol. 15 486–499 (2015).
- 904 53. Baughman, R. P., Lower, E. E. & Du Bois, R. M. Sarcoidosis. in *Lancet* vol. 361
905 1111–1118 (Elsevier Limited, 2003).
- 906 54. Koth, L. L. *et al.* Sarcoidosis blood transcriptome reflects lung inflammation and
907 overlaps with tuberculosis. *Am. J. Respir. Crit. Care Med.* **184**, 1153–1163 (2011).
- 908 55. Maertzdorf, J. *et al.* Common patterns and disease-related signatures in
909 tuberculosis and sarcoidosis. *Proc. Natl. Acad. Sci. U. S. A.* **109**, 7853–7858
910 (2012).
- 911 56. Wahlström, J. *et al.* Analysis of intracellular cytokines in CD4+ and CD8+ lung
912 and blood T cells in sarcoidosis. *Am. J. Respir. Crit. Care Med.* **163**, 115–121
913 (2001).
- 914 57. Rossi, G. A. *et al.* Helper T-lymphocytes in pulmonary sarcoidosis. Functional
915 analysis of a lung T-cell subpopulation in patients with active disease. *Am. Rev.*
916 *Respir. Dis.* **133**, 1086–1090 (1986).
- 917 58. Facco, M. *et al.* Sarcoidosis is a Th1/Th17 multisystem disorder. *Thorax* **66**, 144–
918 150 (2011).
- 919 59. Haynes, W. A. *et al.* Empowering multi-cohort gene expression analysis to
920 increase reproducibility. in *Pacific Symposium on Biocomputing* vol. 0 144–153
921 (World Scientific Publishing Co. Pte Ltd, 2017).
- 922 60. Sweeney, T. E., Haynes, W. A., Vallania, F., Ioannidis, J. P. & Khatri, P. Methods
923 to increase reproducibility in differential gene expression via meta-analysis.
924 *Nucleic Acids Res.* (2017) doi:10.1093/nar/gkw797.
- 925 61. Roy Chowdhury, R. *et al.* A multi-cohort study of the immune factors associated
926 with M. tuberculosis infection outcomes. *Nature* vol. 560 644–648 (2018).
- 927 62. Malherbe, S. T. *et al.* Persisting positron emission tomography lesion activity and
928 Mycobacterium tuberculosis mRNA after tuberculosis cure. *Nat. Med.* **22**, 1094–
929 1100 (2016).
- 930 63. Scriba, T. J. *et al.* Sequential inflammatory processes define human progression
931 from M. tuberculosis infection to tuberculosis disease. *PLOS Pathog.* **13**,
932 e1006687 (2017).

- 933 64. Zak, D. E. *et al.* A blood RNA signature for tuberculosis disease risk: a
934 prospective cohort study. *Lancet* **387**, 2312–2322 (2016).
- 935 65. Flynn, J. L., Goldstein, M. M., Triebold, K. J., Koller, B. & Bloom, B. R. Major
936 histocompatibility complex class I-restricted T cells are required for resistance to
937 *Mycobacterium tuberculosis* infection. *Proc. Natl. Acad. Sci. U. S. A.* **89**, 12013–
938 12017 (1992).
- 939 66. Lalvani, A. *et al.* Human cytolytic and interferon γ -secreting CD8⁺ T lymphocytes
940 specific for *Mycobacterium tuberculosis*. *Proc. Natl. Acad. Sci. U. S. A.* **95**, 270–
941 275 (1998).
- 942 67. Salazar-Onfray, F., López, M. N. & Mendoza-Naranjo, A. Paradoxical effects of
943 cytokines in tumor immune surveillance and tumor immune escape. *Cytokine*
944 *Growth Factor Rev.* **18**, 171–182 (2007).
- 945 68. Li, M. O., Sanjabi, S. & Flavell, R. A. A. Transforming Growth Factor- β Controls
946 Development, Homeostasis, and Tolerance of T Cells by Regulatory T Cell-
947 Dependent and -Independent Mechanisms. *Immunity* **25**, 455–471 (2006).
- 948 69. Jarnicki, A. G., Lysaght, J., Todryk, S. & Mills, K. H. G. Suppression of Antitumor
949 Immunity by IL-10 and TGF- β -Producing T Cells Infiltrating the Growing Tumor:
950 Influence of Tumor Environment on the Induction of CD4⁺ and CD8⁺ Regulatory
951 T Cells. *J. Immunol.* **177**, 896–904 (2006).
- 952 70. Letterio, J. J. & Roberts, A. B. REGULATION OF IMMUNE RESPONSES BY
953 TGF- β . *Annu. Rev. Immunol.* **16**, 137–161 (1998).
- 954 71. Gern, B. H. *et al.* TGF β restricts T cell function and bacterial control within the
955 tuberculous granuloma. *bioRxiv* 696534 (2019) doi:10.1101/696534.
- 956 72. Wong, E. A. *et al.* IL-10 Impairs Local Immune Response in Lung Granulomas
957 and Lymph Nodes during Early *Mycobacterium tuberculosis* Infection. *J.*
958 *Immunol.* **204**, 644–659 (2020).
- 959 73. Havel, J. J., Chowell, D. & Chan, T. A. The evolving landscape of biomarkers for
960 checkpoint inhibitor immunotherapy. *Nature Reviews Cancer* vol. 19 133–150
961 (2019).
- 962 74. Barber, D. L. *et al.* Tuberculosis following PD-1 blockade for cancer
963 immunotherapy. *Sci. Transl. Med.* **11**, (2019).
- 964 75. Anastasopoulou, A., Ziogas, D. C., Samarkos, M., Kirkwood, J. M. & Gogas, H.
965 Reactivation of tuberculosis in cancer patients following administration of immune
966 checkpoint inhibitors: Current evidence and clinical practice recommendations.
967 *Journal for ImmunoTherapy of Cancer* vol. 7 239 (2019).
- 968 76. Tezera, L. B. *et al.* Anti-PD-1 immunotherapy leads to tuberculosis reactivation via
969 dysregulation of TNF- α . *Elife* **9**, (2020).
- 970 77. Hu, Z. *et al.* MetaCyto: A Tool for Automated Meta-analysis of Mass and Flow
971 Cytometry Data. *Cell Rep.* **24**, 1377–1388 (2018).
- 972 78. Newman, M. E. J. Finding community structure in networks using the
973 eigenvectors of matrices. *Phys. Rev. E - Stat. Nonlinear, Soft Matter Phys.* **74**,
974 (2006).
- 975 79. McInnes, L., Healy, J. & Melville, J. UMAP: Uniform Manifold Approximation and
976 Projection for Dimension Reduction. (2018).